scientific reports

Check for updates

OPEN

High-performance machine-learning-based calibration of low-cost nitrogen dioxide sensor using environmental parameter differentials and global data scaling

Slawomir Koziel[1,2]✉, Anna Pietrenko-Dabrowska[2], Marek Wojcikowski[2] & Bogdan Pankiewicz[2]

Accurate tracking of harmful gas concentrations is essential to swiftly and effectively execute measures that mitigate the risks linked to air pollution, specifically in reducing its impact on living conditions, the environment, and the economy. One such prevalent pollutant in urban settings is nitrogen dioxide (NO_2), generated from the combustion of fossil fuels in car engines, commercial manufacturing, and food processing. Its elevated levels have adverse effects on the human respiratory system, exacerbating asthma and potentially causing various lung diseases. However, precise monitoring of NO_2 requires intricate and costly equipment, prompting the need for more affordable yet dependable alternatives. This paper introduces a new method for reliably calibrating cost-effective NO_2 sensors by integrating machine learning with neural network surrogates, global data scaling, and an expanded set of correction model inputs. These inputs encompass differentials of environmental parameters (such as temperature, humidity, atmospheric pressure), as well as readings from both primary and supplementary low-cost NO_2 detectors. The methodology was showcased using a purpose-built platform housing NO_2 and environmental sensors, electronic control units, drivers, and a wireless communication module for data transmission. Comparative experiments utilized NO_2 data acquired during a five-month measurement campaign in Gdansk, Poland, from three independent high-precision reference stations, and low-cost sensor data gathered by the portable measurement platforms at the same locations. The numerical experiments have been carried out using several calibration scenarios using various sets of calibration input, as well as enabling/disabling the use of differentials, global data scaling, and NO_2 readings from the primary sensor. The results validate the remarkable correction quality, exhibiting a correlation coefficient exceeding 0.9 concerning reference data, with a root mean squared error below 3.2 µg/m^3. This level of performance positions the calibrated sensor as a dependable and cost-effective alternative to expensive stationary equipment for NO_2 monitoring.

Keywords Air pollution monitoring, Environmental monitoring, Monitoring platform, Nitrogen dioxide sensors, Low-cost sensors, Sensor calibration, Affine transformation

Nitrogen dioxide (NO_2) stands as a prevalent atmospheric pollutant, originating from internal combustion engines, diverse manufacturing processes (such as nitric acid fabrication, petrol refining, or welding), and food processing. Elevated concentrations pose significant risks to human health, potentially leading to skin infections, respiratory issues, lung cancer, and exacerbation of pre-existing conditions[1–6]. According to standards outlined by the CAFE Directive[7], the average annual concentration should not surpass 40 µg/m^3, with hourly concentrations not exceeding 200 µg/m^3 for more than 18 h annually. Similar yet more stringent guidelines are proposed by the World Health Organization (WHO)[8]. Nevertheless, NO_2 concentrations certain areas exceed these prescribed limits[54,55].This issue is especially prominent in densely urbanized regions, notably associated with routes of car transportation. The economic consequences of air pollution, including NO_2, are substantial[9]. For instance, in

[1]Engineering Optimization & Modeling Center, Reykjavik University, 102 Reykjavík, Iceland. [2]Faculty of Electronics, Telecommunications and Informatics, Gdansk University of Technology, 80-233 Gdańsk, Poland. ✉email: koziel@ru.is

2016, NO_2-related costs in China alone amounted to nearly 30 billion US dollars[2]. NO_x pollution contributes to the creation of photochemical smog, the development of acid rain, and the eutrophication of aquatic ecosystems, ultimately leading to ecological deterioration in water reservoirs[10]. Additionally, elevated NO_x concentrations heighten O_3 levels, negatively impacting agriculture.

Traditional methods for monitoring NO_2 typically rely on cumbersome and fixed equipment, demanding specific installation conditions and frequent upkeep. The expenses associated with their procurement and maintenance are usually considerable. Various measurement techniques include photofragment chemiluminescence (which is sensitive but necessitates regular calibration)[11], long-range differential optical absorption spectroscopy (also sensitive but limited to spatially extended measurements)[12], laser-induced fluorescence (highly sensitive and rapid but requires a vacuum system and a pulsed laser)[13], and cavity ring spectroscopy (requires no calibration, facilitating portable measurements)[14].

The drawbacks associated with traditional monitoring stations have spurred the development of cost-effective detection methods that are portable, easy to deploy, and maintain. These approaches aim to improve the spatial resolution of air quality monitoring, particularly crucial in urban areas characterized by diverse air pollutant distributions[15–17]. However, inexpensive sensors often face limitations in reliability[18–20], attributed to factors like instability[21], inconsistent manufacturing[22,23], susceptibility to cross-sensitivity with other gases[24–26], and sensitivity to environmental conditions such as temperature or humidity[27,28]. Despite these limitations, deploying cost-effective sensors in large numbers can complement sparsely located reference stations. Additionally, they offer affordable air pollutant detection options for regions with limited resources[29] and serve in establishing sensor networks[30,31] (for instance, on ground or aerial vehicles[32,33]), playing a key role in developing integrated air quality monitoring systems.

In recent years, significant research endeavours have focused on enhancing the reliability of low-cost sensors through appropriate calibration methods. These techniques are broadly classified into two categories: laboratory and field-based approaches[34]. While laboratory calibration is theoretically more accurate, its practical utility is limited as real-world conditions seldom match controlled laboratory settings[18,19]. Consequently, the majority of studies prioritize field calibration, leveraging reference data obtained from public monitoring stations. Numerical modelling for sensor correction encompasses various regression and machine learning methods, with the latter including neural networks. For instance, in[35], multivariate linear regression (MLR), support vector regression (SVR), and random forest regression (RFR) were utilized to calibrate electrochemical NO and NO_2 sensors using temperature and humidity data. In another study[36], ridge regression, a linear statistical learning algorithm, RFR, Gaussian process regression (GPR), and MLR were employed to rectify readings from low-cost NO_2 and PM_{10} sensors based on temperature and humidity. Successful calibration using MLR was demonstrated in[37] for a chemiluminescence NO-NO_2-NO_x analyser, also utilizing temperature and humidity data. Further studies focusing on regression-based sensor calibration can be found in[38–40].

In recent times, artificial neural networks and other machine learning techniques have proven to be reliable tools for correcting low-cost sensors. Calibration of CO, NO_2, O_3, and SO_2 sensors has been achieved using single linear regression (SLR), multivariate linear regression (MLR), random forest regression (RFR), and long short-term memory networks (LSTM) in[29]. The outcomes highlighted the superior performance of LSTM over all regression-based algorithms. Another study[15] employed convolutional neural networks (CNNs) and recurrent neural networks (RNNs) to calibrate sensors based on historical time series data. Calibration of commercial CO and O_3 sensors, utilizing temperature and humidity data, supported the advantages of CNN/RNN over various regression methods like linear regression (LR), support vector regression (SVR), or LSTM combined with CNN. Other types of artificial neural network (ANN) models used for calibration purposes include Bayesian neural networks[41], shallow neural networks[42], and dynamic neural networks[43,44].

This article aims to introduce an innovative method for precisely calibrating cost-effective NO_2 sensors. Our approach integrates machine learning, specifically neural network surrogates, global data scaling, and an expanded range of correction model inputs. These inputs encompass environmental parameters (like temperature, humidity, atmospheric pressure), their differentials, along with readings from both primary and supplementary low-cost NO_2 sensors. The neural network model is trained to accurately represent additive and multiplicative correction coefficients based on the aforementioned environmental and auxiliary variables. Global scaling is then applied to enhance the correlation between reference and calibrated sensor data by employing appropriate affine transformations established using the complete set of training samples. The utilization of differentials has demonstrated improved reliability in sensor calibration by linking correction coefficients to temporal changes in parameters such as temperature, humidity, or NO_2 readings from the sensor in question. To verify our methodology, it was applied to a custom-built autonomous monitoring platform incorporating nitrogen dioxide and environmental detectors, as well as electronic circuitry controlling system operations and implementing measurement and data transfer protocols. Reference data was collected over five months from public high-precision stations in Gdansk, Poland. The results affirm exceptional calibration efficiency, showcasing a correlation coefficient exceeding 0.9 with reference data, and a measurement accuracy quantified by RMSE below 3.2 $\mu g/m^3$. Additionally, all developed algorithmic tools have demonstrated their effectiveness in enhancing the quality of the calibration process. The achieved performance of the corrected sensor validates its suitability for cost-efficient and reliable NO_2 monitoring.

Autonomous NO_2 monitoring platform: reference data acquisition

The calibration methodology we propose has been implemented on a specially designed autonomous monitoring platform, detailed in this section. Here, we provide a brief overview of the hardware and sensors integrated into this system. The specific machine-learning-based calibration process for the NO_2 sensor will be extensively discussed in section "Machine learning and global data scaling for reliable sensor calibration".

Autonomous monitoring platform

The air pollution data is collected using a tailored microprocessor-based hardware platform. This system integrates multiple sensors for monitoring environmental parameters such as temperature, humidity, and atmospheric pressure, along with three nitrogen dioxide sensors (one primary and two auxiliary). Additionally, it includes a global system for mobile communication (GSM) modem for wireless transmission of measurement results to the cloud. The automated data acquisition protocols utilize off-the-shelf components managed by the microprocessor system BeagleBone® Blue[45]. This Linux-based computer board features a 1 GHz ARM® Cortex-A8 processor, 512 MB DDR3 RAM, 4 GB eMMC memory, and a data storage unit. A rechargeable 7.4 V/4400 mA battery ensures system operation for a minimum of twenty hours without external power. The BeagleBone board integrates serial input/output ports used for connecting various modules, such as the cellular connectivity module and multiple low-cost gas and environmental sensors. The platform incorporates three NO_2 sensors alongside temperature, humidity, and pressure detectors. Figure 1 illustrates the platform's block diagram and the pertinent sensor information. Software drivers for the hardware modules are developed in Python3. Measurement results, transmitted via the GSM modem to the cloud, are accessible online.

The entire system has been mounted on a custom base plate crafted from polyethylene terephthalate, as depicted in Fig. 2. The gas sensors (SGX, ST, MICS) are positioned in close proximity to each other (refer to Fig. 2a), alongside the environmental detectors that assess their operational surroundings. An auxiliary environmental parameter sensor was situated at the device's edge to measure external temperature and humidity. There is a distinction between internal and external temperature/humidity due to the heat generated by the processor board.

Additionally, the system includes an Intel USB Stick module, capable of supporting computations for implementing calibration algorithms. The entire platform is enclosed within a polyethylene terephthalate weatherproof housing, as shown in Fig. 2c. The measurements were taken in the period March to August 2023 with the data recorded hourly. The total number of readings exceeds 10,000.

Reference data

To calibrate the low-cost sensor mentioned in section "Autonomous monitoring platform", we gathered high-quality reference data from a network of public monitoring stations situated in Gdansk, Poland. These stations, established and maintained by the ARMAG Foundation[50], are equipped with air-conditioned containers and high-performance measuring devices. They undergo regular supervision and calibration. Figure 3a illustrates the spatial distribution of the reference stations, while Fig. 3b showcases a photograph of one such station. The equipment utilized for NO-NO_2-NO_x monitoring is itemized in Fig. 3c.

The air quality data generated by ARMAG is available to the public free of charge via the foundation's website (https://armaag.gda.pl/en/). These measurements are conducted hourly, and the results are showcased on the website for a duration of three days. To collect data over more extended periods, a custom script has been developed. This script automatically downloads the information into a text file stored on a dedicated server.

Data acquisition

Validation of the presented calibration procedure involves data obtained from both the reference stations (as detailed in section "Reference data") and the monitoring platforms outlined in section "Autonomous monitoring platform". This data spans from March to August 2023 and is recorded hourly, totalling over 10,000 samples. Approximately ninety percent of this dataset was utilized to establish the calibration models (neural network,

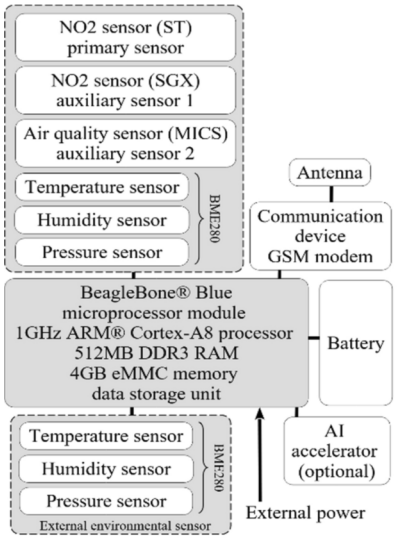

(a)

Sensor	Purpose
SGX-7NO2	NO_2 electrochemical sensor (SGX Sensortech [46]), denoted as SGX
7E4-NO2	NO_2 electrochemical sensor (SemaTech [47]), denoted as ST
MiCS 2714	Compact MOS air quality sensor (SGX Sensortech [48]), for detecting NO_2 and hydrogen, denoted as MICS
BME280	Environmental sensor (Bosch Sensortech [49]) capable of measuring ambient temperature and humidity together with atmospheric pressure mounted on PCB near the NO_2 sensors targeted to measure the operating conditions of the NO_2 sensors (internal)
BME280	Environmental sensor (Bosch Sensortech [49]) placed at the very edge of the enclosure to measure the parameters of air surrounding the system (external)

(b)

Fig. 1. Autonomous air monitoring platform: (**a**) block diagram, (**b**) included sensors.

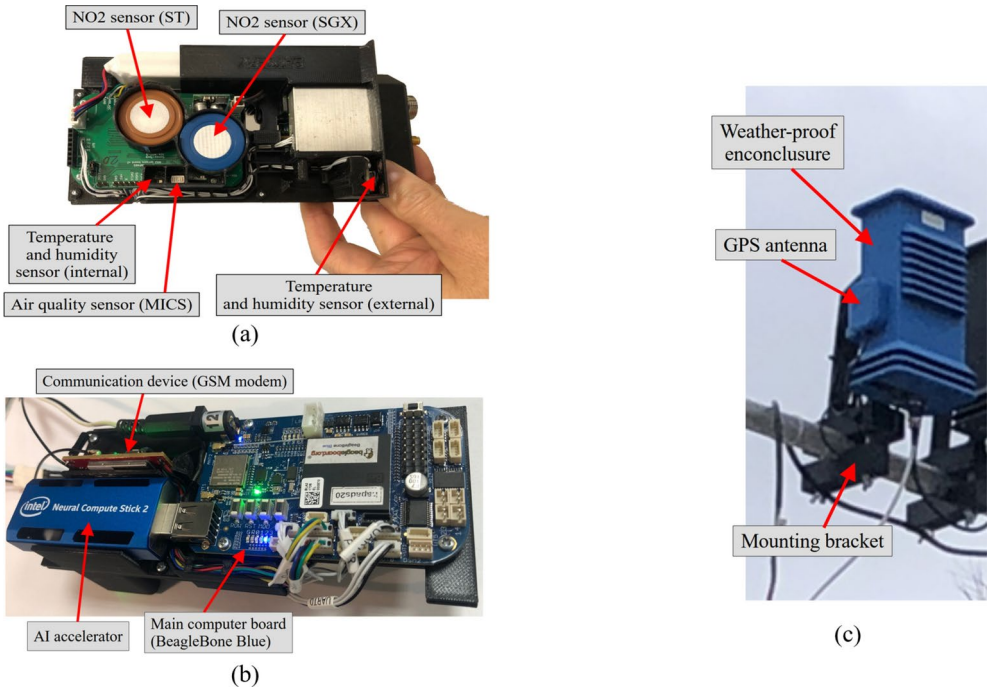

Fig. 2. Autonomous monitoring platform: (**a**) internals (top view), (**b**) internals (bottom view), (**c**) mounted at the reference station.

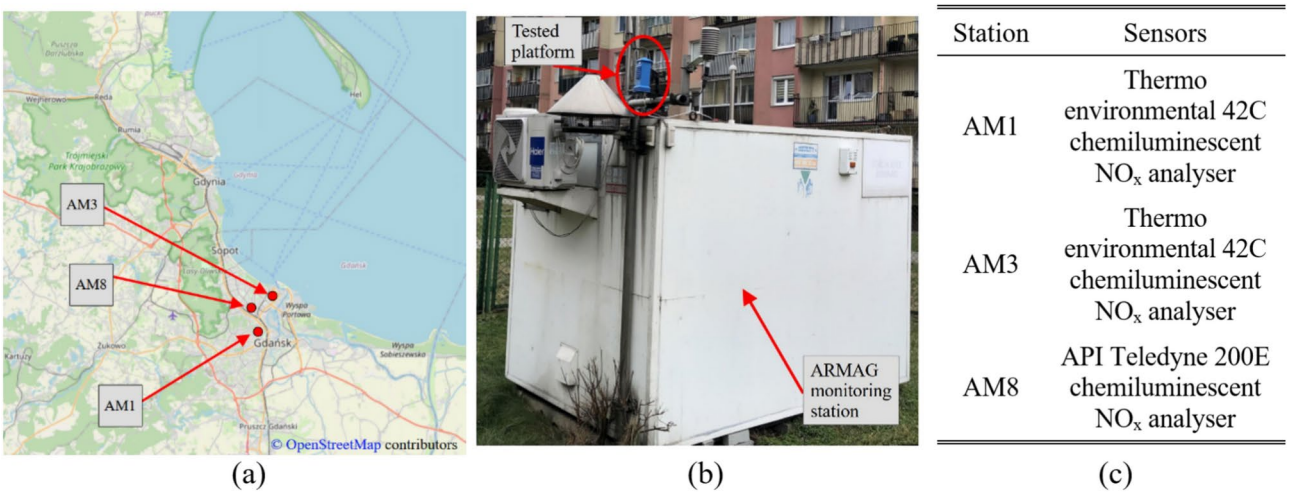

Station	Sensors
AM1	Thermo environmental 42C chemiluminescent NO_x analyser
AM3	Thermo environmental 42C chemiluminescent NO_x analyser
AM8	API Teledyne 200E chemiluminescent NO_x analyser

(c)

Fig. 3. Reference monitoring stations of the ARMAG foundation used to acquire reference data: (**a**) station locations in the city of Gdansk (map data from OpenStreetMap[57]), (**b**) photograph of the selected station with the proposed low-cost platform mounted in the vicinity, (**c**) NO_x sensors installed on the stations.

global data scaling). The remaining data, specifically $N_t = 3 \times 336 = 1008$ samples, were reserved for testing purposes. These test samples correspond to three distinct two-week periods at three different sensor locations (Station 1, April 1–15; Station 2, July 15–29; Station 3; July 1–14).

Machine learning and global data scaling for reliable sensor calibration

This section presents the proposed methodology for calibrating the low-cost NO_2 sensor. The key components of this approach encompass a combined additive and multiplicative correction for NO_2 readings, the utilization of a neural network (NN) surrogate for predicting correction coefficients based on detected environmental parameters and their differentials, and global affine scaling to improve the correlation between reference and calibrated sensor data. The content is structured as follows. Section "Sensor calibration: problem formulation" formulates the calibration problem and discusses the NO_2 and environmental variables involved in the process. Section "Affine response correction of low-cost sensor" defines a combined additive and multiplicative correction

scheme. Section "Sensor calibration by machine learning: neural network surrogate" elaborates on the surrogate modelling technique employed in the calibration procedure. The use of differentials as auxiliary correction variables is detailed in section "Environmental parameter differential as additional calibration inputs". Section "Global data correlation enhancement" outlines the process of global data scaling. Finally, section "Nitrogen dioxide detection using calibrated sensor: complete operating flow" summarizes the complete operational flow of NO_2 monitoring using the calibrated sensor.

Sensor calibration: problem formulation

Calibrating the low-cost sensor involves utilizing data acquired from the reference stations mentioned in section "Reference data". As previously indicated, measurements are taken hourly. The data collected from the autonomous platforms in section "Autonomous NO_2 monitoring platform: reference data acquisition" corresponds to the same time intervals and includes NO_2 readings from the primary and auxiliary sensors, alongside environmental variables like temperature, humidity, and atmospheric pressure. Figure 4 presents a visualization of pertinent outputs from both the reference stations and the low-cost sensors, along with the corresponding notation used throughout (refer to Fig. 4c). Notably, differences exist between internal and external temperature and humidity due to the electronic circuitry's heat within the platform, causing the operating conditions of the NO_2 sensors to vary from those outside the unit. Considering both external and internal parameters can enhance calibration reliability. While the auxiliary NO_2 sensors have limited reliability, incorporating their readings as inputs in the calibration models provides indirect yet valuable insights into the factors affecting the primary sensor, such as cross-sensitivity to other gases.

The overall data is divided into the training set (N_0 samples), and the testing set (N_t samples); N_t is set to approximately ten percent of the total number of samples N. The reference training and testing data will be denoted as $\{y_{r0}^{(j)}\}$, $j=1, \ldots, N_0$, and $\{y_{rt}^{(j)}\}$, $j=1, \ldots, N_t$, respectively. The low-cost sensor data is split the same way. We have $\{y_{s0}^{(j)}\}$, $j=1, \ldots, N_0$–sensor's NO_2 measurements (training data), and $\{y_{st}^{(j)}\}$, $j=1, \ldots, N_t$–sensor's NO_2 measurements (testing data). The auxiliary data (the inputs of the calibration models) is $\{\boldsymbol{z}_{s0}^{(j)}\}$, $j=1, \ldots, N_0$, where $\boldsymbol{z}_{s0}=[T_{o0}^{(j)}T_{i0}^{(j)}H_{o0}^{(j)}H_{i0}^{(j)}P_0^{(j)}S_{10}^{(j)}S_{20}^{(j)}]^T$, and $\{\boldsymbol{z}_{st}^{(j)}\}$, $j=1, \ldots, N_t$, $\boldsymbol{z}_{st}=[T_{ot}^{(j)}T_{it}^{(j)}H_{ot}^{(j)}H_{it}^{(j)}P_t^{(j)}S_{1t}^{(j)}S_{2t}^{(j)}]^T$.

Low-cost sensor calibration is performed using the training datasets $\{y_{r0}^{(j)}\}$, $\{y_{s0}^{(j)}\}$, and $\{\boldsymbol{z}_{s0}^{(j)}\}$, $j=1, \ldots, N_0$. The correction coefficients are denoted as $C(y_s,\boldsymbol{z}_s;\boldsymbol{p})$, cf. Figure 5, where $\boldsymbol{p}$ stands for an aggregated vector of calibration model hyper-parameters. The calibrated sensor output will be denoted as $y_c=F_{CAL}(y_s,C(y_s,\boldsymbol{z}_s;\boldsymbol{p}))$. Having established the notation, the calibration task can be formulated as

$$\boldsymbol{p}^* = \arg\min_{\boldsymbol{p}} \sqrt{\sum_{j=1}^{N_0} \left(y_{r0}^{(j)} - F_{CAL}\left(C(y_{s0}^{(j)}, \boldsymbol{z}_{s0}^{(j)}, \boldsymbol{p}) \right) \right)^2} \tag{1}$$

Put simply, the objective is to optimize the calibration model's hyper-parameters in a manner that aligns the NO_2 readings from the reference and corrected low-cost sensors as closely as feasible in the least-square sense across the training set. The quality of the calibrated sensor will be evaluated using the correlation coefficient r, and the root mean squared error (RMSE), both defined in Fig. 6.

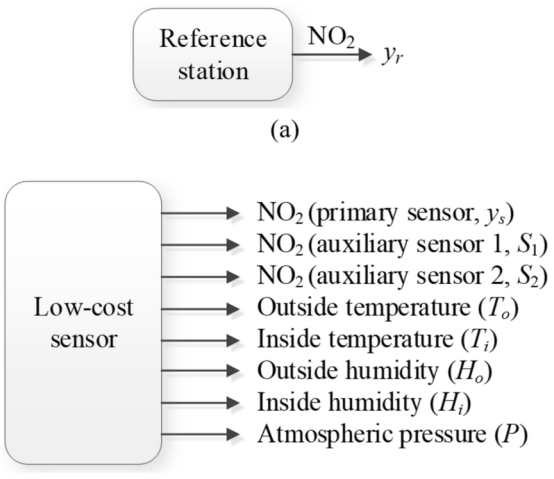

Measurement station	Data type	Symbol[#]
Reference	NO_2 concentration	$y_r^{(j)}, j=1, \ldots, N$
Low-cost platform of Section 2	NO_2 concentration (primary sensor: ST)	$y_s^{(j)}, j=1, \ldots, N$
	NO_2 concentration (auxiliary sensor 1: SGX)	$S_1^{(j)}, j=1, \ldots, N$
	NO_2 concentration (auxiliary sensor 2: MICS)	$S_2^{(j)}, j=1, \ldots, N$
	Outside temperature	$T_o^{(j)}, j=1, \ldots, N$
	Inside temperature	$T_i^{(j)}, j=1, \ldots, N$
	Outside humidity	$H_o^{(j)}, j=1, \ldots, N$
	Inside humidity	$H_i^{(j)}, j=1, \ldots, N$
	Atmospheric pressure	$P^{(j)}, j=1, \ldots, N$

[#]N is the total number of samples from all measurement locations.

(c)

Fig. 4. NO_2 measurement: (**a**) using the reference station (y_r); (**b**) using the low-cost sensor under calibration (y_s). The sensor also produces auxiliary outputs: auxiliary NO_2 readings (S_1 and S_2), outside and inside temperature (T_o and T_i, respectively), outside and inside humidity (H_o and H_i, respectively), and atmospheric pressure (P); (**c**) symbols of data produced by the reference station and low-cost sensor.

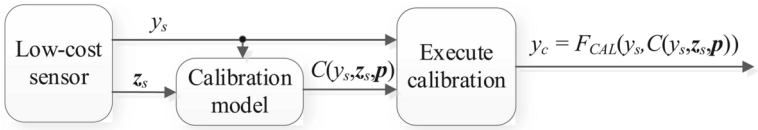

Fig. 5. Calibration of the low-cost sensor. Auxiliary data and sensor output y_s are used to obtain the correction coefficients $C(y_s,\boldsymbol{z}_s,\boldsymbol{p})$, which are then used to compute the corrected sensor output y_c, see sections "Affine response correction of low-cost sensor" through "Nitrogen dioxide detection using calibrated sensor: complete operating flow" for details.

Correlation coefficient:

$$r = \frac{\sum_{j=1}^{N_t}\left(y_c^{(j)} - \bar{y}_c\right)\left(y_{rt}^{(j)} - \bar{y}_{rt}\right)}{\sqrt{\sum_{j=1}^{N_t}\left(y_c^{(j)} - \bar{y}_c\right)^2 \sum_{j=1}^{N_t}\left(y_{rt}^{(j)} - \bar{y}_{rt}\right)^2}} \tag{2}$$

Root-mean-square error:

$$RMSE = \sqrt{\sum_{j=1}^{N_t} \frac{\left(y_c^{(j)} - y_{rt}^{(j)}\right)^2}{N_t}} \tag{3}$$

where $y_c^{(j)}$ and $y_{rt}^{(j)}$, $j = 1, \ldots, N_t$, are the corrected sensor and reference NO_2 readings, whereas the quantities with bars are the respective mean values.

Fig. 6. Definitions of correlation coefficient r and RMSE.

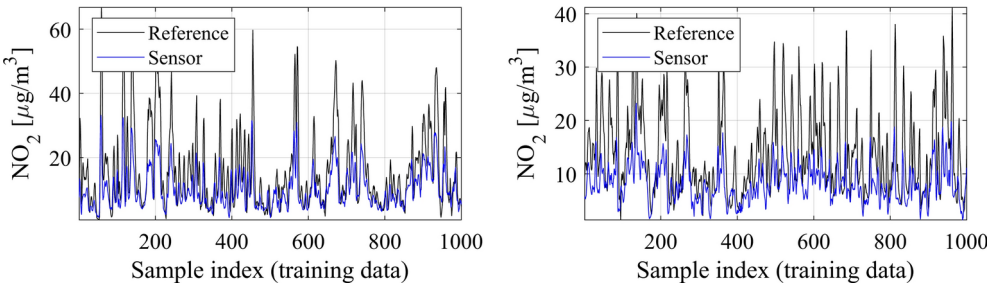

Fig. 7. Selected sub-sets of the reference and low-cost sensor training data. As the typical amplitude of sensor data variations is lower than for the reference, multiplicative scaling with coefficient $A > 1$ may be beneficial in improving the calibration process quality.

Affine response correction of low-cost sensor

Conventional correction methods typically involve modelling the disparities between the reference and low-cost sensor readings. In contrast, our approach employs affine scaling, which integrates both additive and multiplicative correction. The inclusion of a multiplicative scaling factor larger than unity is motivated by the observation that typical variations in the reference data surpass those in the sensor measurements, as depicted in Fig. 7. Consequently, this scaling method contributes to enhancing the reliability of the calibration process.

Figure 8 outlines the specifics of this correction scheme. To ensure $A^{(j)} > 1$, the hyper-parameter α (refer to Eqs. (9) and (10)) must be strictly less than unity. For our purposes, α is adjusted concurrently with the neural network calibration model identification (refer to section "Sensor calibration by machine learning: neural network surrogate"). Based on preliminary experiments, a suitable value for α is found to be 0.8, which is utilized in the experiments detailed in section "Results and discussion".

Sensor calibration by machine learning: neural network surrogate

In this study, the main calibration model adopted is a neural network (NN), specifically a multi-layer perceptron (MLP)[51,52]. The MLP comprises three fully-connected hidden layers, each containing twenty neurons and employing a sigmoid activation function. Training of the model is carried out with a backpropagation Levenberg–Marquardt routine[53] (setup: maximum of 1000 epochs, performance evaluation via mean-square error (MSE), and a random division of training/testing data). The architecture of the model is depicted in Fig. 9. The complete calibration procedure, including the MLP model, has been implemented in Matlab using the functionalities of the Statistics and Machine Learning Toolbox[56].

Basic sensor correction scheme:

$$y_c = A(y_s + D) \tag{4}$$

where y_c is the corrected sensor reading, whereas both correction coefficients are produced by the calibration function $C(y_s, \boldsymbol{z}_s, \boldsymbol{p})$.

Given (4), the calibration function takes the form of

$$C(y_s, \boldsymbol{z}_s, \boldsymbol{p}) = [A(y_s, \boldsymbol{z}_s, \boldsymbol{p}) + D(y_s, \boldsymbol{z}_s, \boldsymbol{p})]^T \tag{5}$$

and

$$y_c = F_{CAL}\left(y_s, C(y_s, \boldsymbol{z}_s, \boldsymbol{p})\right) = A(y_s, \boldsymbol{z}_s, \boldsymbol{p})\left[y_s + D(y_s, \boldsymbol{z}_s, \boldsymbol{p})\right] \tag{6}$$

Calibration coefficient identification: parameters A and D are computed for each training sample, so that we have

$$y_{r0}^{(j)} = A^{(j)}(y_{s0}^{(j)} + D^{(j)}) \tag{7}$$

for $j = 1, \ldots, N_0$, and the problem (1) is replaced by

$$\boldsymbol{p}^* = \arg\min_{\boldsymbol{p}} \left\| [\boldsymbol{A}_0 \ \boldsymbol{D}_0] - \boldsymbol{C}_0(\boldsymbol{p}) \right\|^2 \tag{8}$$

where

$$\boldsymbol{A}_0 = \begin{bmatrix} A^{(1)} \\ \vdots \\ A^{(N_0)} \end{bmatrix}, \quad \boldsymbol{D}_0 = \begin{bmatrix} D^{(1)} \\ \vdots \\ D^{(N_0)} \end{bmatrix}, \quad \boldsymbol{C}_0(\boldsymbol{p}) = \begin{bmatrix} C(y_{s0}^{(1)}, \boldsymbol{z}_{s0}^{(1)}, \boldsymbol{p})^T \\ \vdots \\ C(y_{s0}^{(N_0)}, \boldsymbol{z}_{s0}^{(N_0)}, \boldsymbol{p})^T \end{bmatrix} = \begin{bmatrix} A(y_{s0}^{(1)}, \boldsymbol{z}_{s0}^{(1)}, \boldsymbol{p}) & D(y_{s0}^{(1)}, \boldsymbol{z}_{s0}^{(1)}, \boldsymbol{p}) \\ \vdots & \vdots \\ D(y_{s0}^{(N_0)}, \boldsymbol{z}_{s0}^{(N_0)}, \boldsymbol{p})^T & D(y_{s0}^{(N_0)}, \boldsymbol{z}_{s0}^{(N_0)}, \boldsymbol{p})^T \end{bmatrix} \tag{9}$$

and

Uniqueness problem: Solution to (7) is not unique. Here, a regularization is implemented by introducing a calibration hyper-parameter $0 \le \alpha \le 1$, which 'distributes' the weights between additive and multiplicative correction. We have

$$D^{(j)} = \alpha\left[y_{r0}^{(j)} - y_{s0}^{(j)}\right] \quad \text{and} \quad A^{(j)} = \frac{y_{r0}^{(j)}}{y_{s0}^{(j)} + \alpha(y_{r0}^{(j)} - y_{s0}^{(j)})} \tag{10}$$

Fig. 8. Affine correction of low-cost sensor.

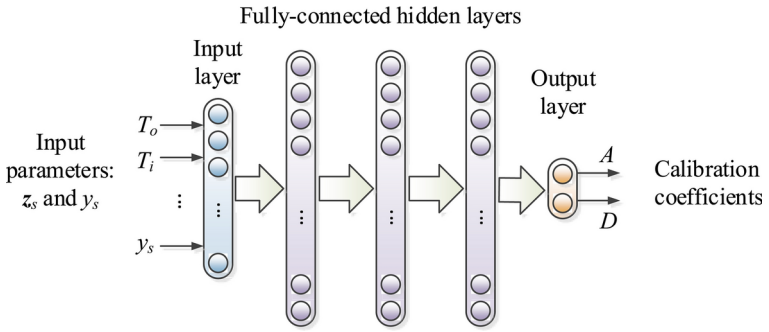

Fig. 9. Neural network surrogate used as the primary calibration model. Here, a multi-layer perceptron (MLP) is employed with three fully-connected hidden layers.

The deliberate simplicity in the NN setup serves several purposes. Firstly, it expedites the identification of the network's hyper-parameters, enabling exploration of various MLP variations efficiently. Secondly, with a substantial number of training samples, the neural network effectively operates as a regression model. Consequently, its sensitivity to the number of layers and neurons remains constrained. Lastly, the straightforward structure of the network facilitates noise smoothing, a beneficial aspect for handling inherent noise present in both the reference and sensor readings. Remember that the surrogate model inputs encompass environmental parameters and supplementary NO_2 readings, represented as vector $\boldsymbol{z}_s$, along with the primary NO_2 measurements y_s. Meanwhile, the model outputs consist of the affine scaling coefficients A and D. In section "Results and discussion", we will explore restricted inputs—different subsets of $\boldsymbol{z}_s$—to assess how the input configuration affects the reliability of the calibration process.

Environmental parameter differential as additional calibration inputs

Environmental parameters (inside/outside temperature, humidity, atmospheric pressure) as well as supplementary NO_2 readings provide reasonably comprehensive data to conduct the calibration process. Nonetheless, in this study, we also explore additional information which can be extracted from local variations of the mentioned parameters. In particular, we will consider differentials

$$\Delta y_s^{(j)} = \frac{y_s^{(j)} - y_s^{(j-1)}}{\Delta t} \tag{11}$$

where Δt is the time between subsequent measurements (here, one hour), whereas $y_s^{(j-1)}$ is assumed to be the measurement taken Δt before $y_s^{(j-1)}$ (normally, both training and testing data comes as time series with readings spaced Δt in terms of time). Differentials for environmental parameters are defined the same way, e.g.,

$$\Delta T_o^{(j)} = \frac{T_o^{(j)} - T_o^{(j-1)}}{\Delta t} \tag{12}$$

$$\Delta H_o^{(j)} = \frac{H_o^{(j)} - H_o^{(j-1)}}{\Delta t} \tag{13}$$

$$\Delta P^{(j)} = \frac{P^{(j)} - P^{(j-1)}}{\Delta t} \tag{14}$$

Similar definitions hold for inside temperature and humidity, T_i and H_i, respectively.

Computing the differential only require storing one set of measurements (from the previous reading instance). At the same time, the differentials, especially $\Delta y_s^{(j)}$, account for the dynamics of NO_2 concentration, and are indicative of upcoming changes, including quantification of measurement level variability. Similarly, differentials of environmental variables may carry useful information concerning the dynamics of explicit or implicit factors (e.g., cross-sensitivity to other gases). Information carried therein can be embedded into the neural network surrogate (when treating the differentials as additional inputs) and used to improve the calibration quality.

For illustration purposes, Fig. 10 shows a selected sequence of the training data (raw sensor's NO_2 readings) along with its differentials. Figure 11 shows the effects of incorporating the differentials as additional surrogate model inputs in the calibration process. The modified calibration procedure incorporating differentials, collectively denoted as $\Delta \boldsymbol{z}_s$, has been shown in Fig. 12.

Global data correlation enhancement

To complement the machine learning (ML)-based calibration method detailed in sections "Sensor calibration: problem formulation" to "Environmental parameter differential as additional calibration inputs", this section introduces an additional global data scaling process. The aim is to mitigate a systematic offset that might arise during the calibration conducted in the least-square sense (cf. (1)). This offset typically correlates with the measured NO_2 level, as depicted in Fig. 13a and b for a specific subset of the training data. Although the ML-based calibration appears to align the reference and low-cost sensor readings acceptably (cf. Fig. 13a), re-examining the data after arranging the reference NO_2 levels exposes these existing offsets. This discrepancy also influences the scatter plot (bottom panel of Fig. 11b), which shows a slight skewness.

Red uction of the offset can be achieved through affine transformation of the smoothened sensor readings. Let us denote as $\boldsymbol{y}_r$ the ordered reference data vector (a red line in Fig. 13b), and by $\boldsymbol{y}_c$ the corresponding calibrated low-cost sensor data (a blue line in Fig. 13b). Also, let $S_m(\boldsymbol{y}_c)$ be the smoothened $\boldsymbol{y}_c$. Aggressive smoothing S_m would produce a monotonically increasing curve which represents (local) mean values for $\boldsymbol{y}_c$. Global data scaling is then conducted by means of a transformation similar to (2), i.e., we have

$$y_{c,G}^{(j)} = A_G(y_c^{(j)} + D_G) \tag{15}$$

for $j = 1, \ldots, N_0$, where A_G and D_G are found as

$$[A_G \; D_G] = \arg\min_{[A \; D]} \|y_r - A\,(S_m(y_c) + D)\| \tag{16}$$

Note that A_G and D_G are determined based on complete training data vectors and do not rely on any environmental or auxiliary parameters. Figure 13c illustrates the impact of the global data scaling. Notably, there is a significant

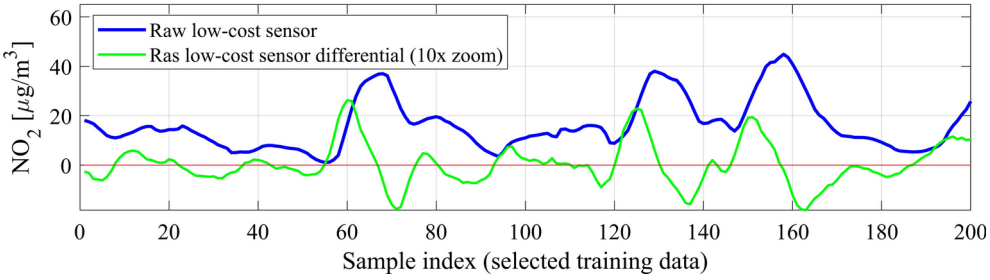

Fig. 10. Exemplary training data sequence (NO_2 readings from the low-cost sensor) and its corresponding differentials (11). Differentials are indicative of temporal variability of the sensor readings and may improve calibration quality upon being embedded into the NN calibration surrogate.

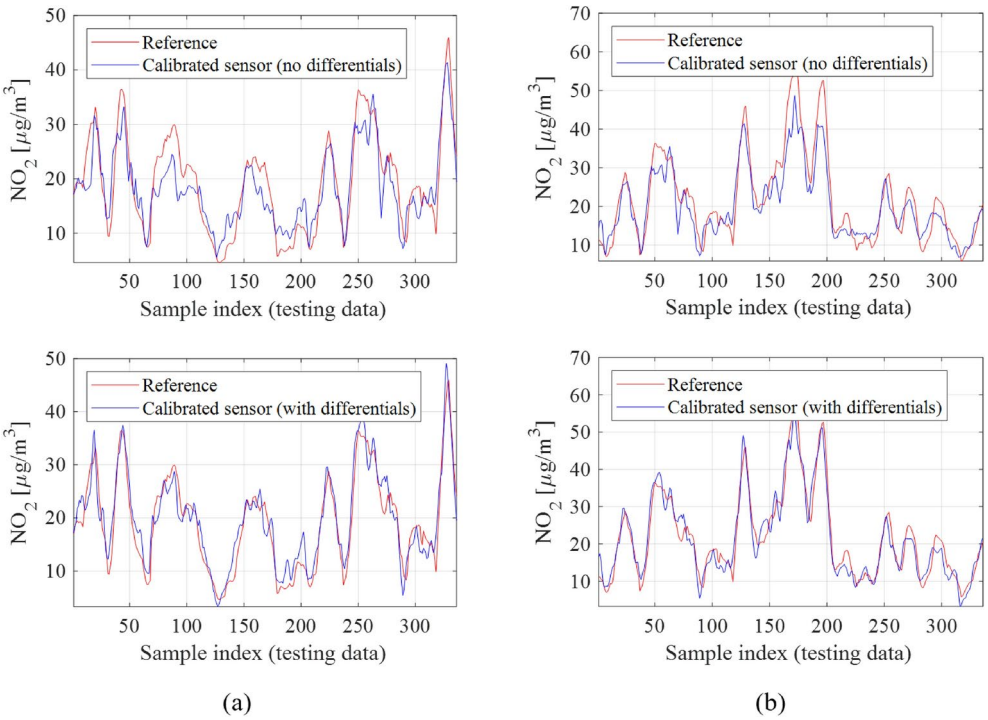

Fig. 11. The effects of incorporating differentials as input variables in the calibration process, shown for two selected sequences of testing data: (**a**) sequence 1, (**b**) sequence 2. As it can be observed including differentials (here, of all environmental variables and the primary NO_2 readings from the low-cost sensor) noticeably improves data alignment.

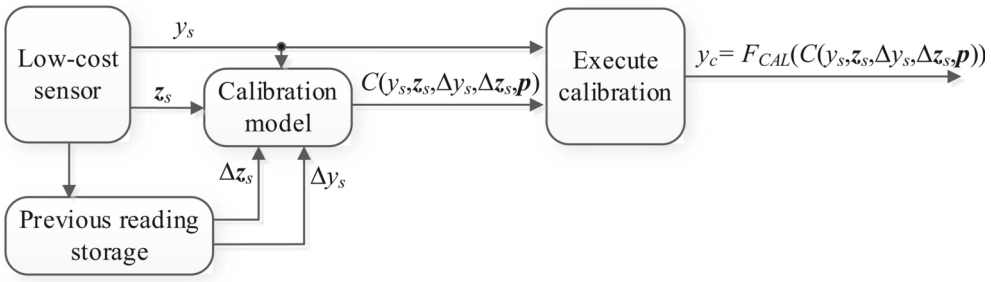

Fig. 12. Calibration of the low-cost sensor with differentials used as additional calibration model inputs. Auxiliary data and sensor output y_s are used to obtain the correction coefficients $C(y_s,\boldsymbol{z}_s,\Delta y_s,\Delta \boldsymbol{z}_s,\boldsymbol{p})$, used to compute the corrected sensor output y_c.

reduction in the offset along with improved symmetry in the scatter plot. In the specific example considered, this correction enhances the correlation coefficient from 0.93 to 0.95 and decreases the RMSE from 2.1 to 1.8 μg/m^3. While the advantages might be somewhat less favourable for testing data, they remain valuable, as detailed in section "Results and discussion".

Nitrogen dioxide detection using calibrated sensor: complete operating flow

The comprehensive calibration process for the low-cost sensor involves the methodologies outlined in sections "Affine response correction of low-cost sensor" through "Global data correlation enhancement". The initial phase predicts the (local) correction coefficients using the neural network, considering the auxiliary vector $\boldsymbol{z}_s$, the actual NO_2 reading y_s from the low-cost sensor, and their differentials. This results in the intermediate outcome y_c, achieved by applying the affine correction (4), (5). Subsequently, the final corrected NO_2 reading is derived by implementing the global data correlation scheme (14), (15). The flow diagram illustrating this process is presented in Fig. 14.

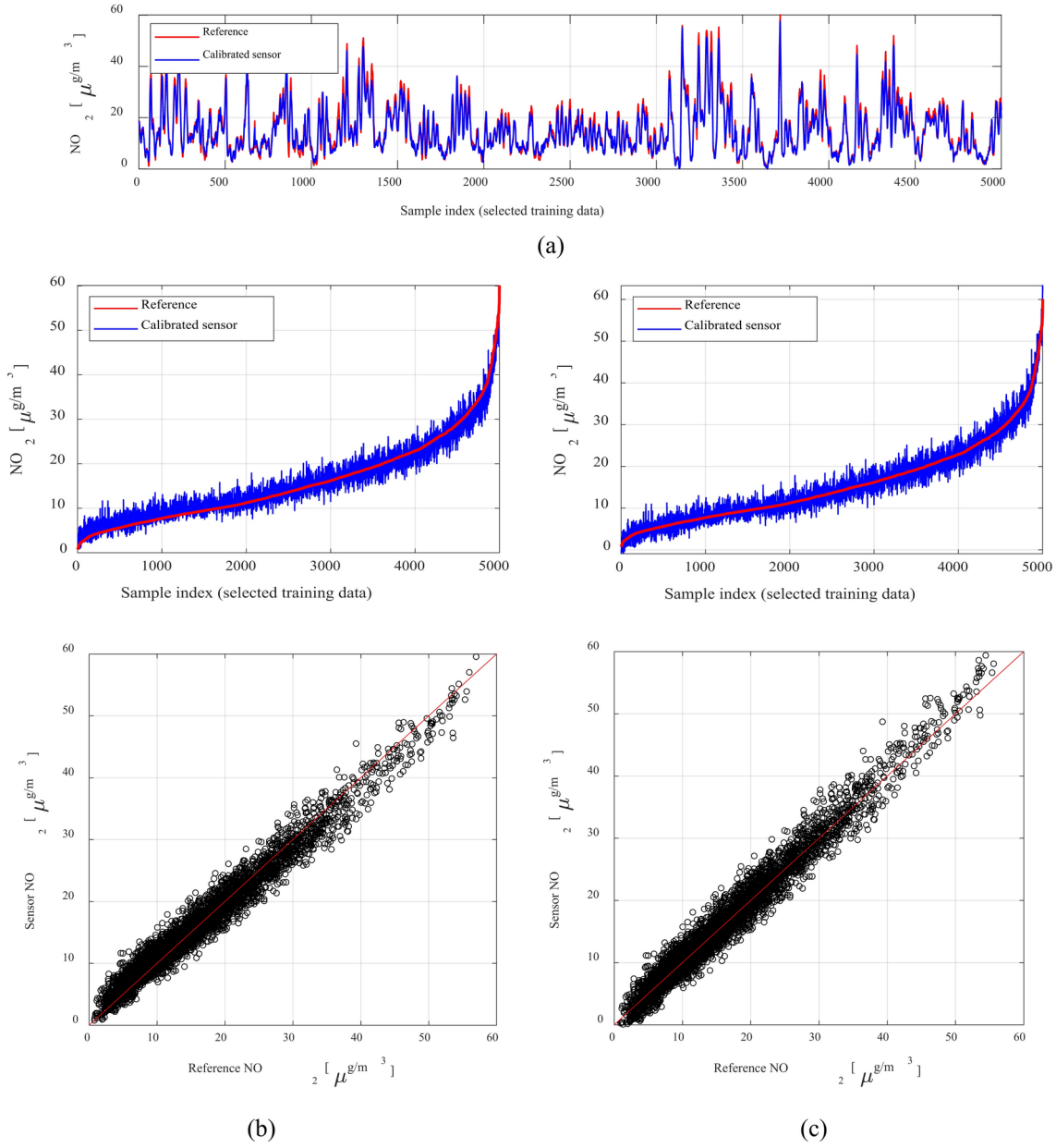

Fig. 13. Global data scaling: (**a**) selected training data subset; (**b**) same data but ordered w.r.t. increasing NO_2 reference readings (top) and corresponding scatter plot (bottom); despite good alignment as shown in Fig. 11a, a systematic level-dependent offset is observed; (**c**) same data but plotted after applying global data scaling; a significant reduction of the systematic offset can be observed along with improved symmetry of the scatter plot. In this case, the correction leads to improving the correlation coefficient from 0.93 to 0.95 and reduction of RMSE from 2.1 to 1.8 $\mu g/m^3$.

Results and discussion

In this section, we explore the results obtained from the calibration methodology introduced in section "Machine learning and global data scaling for reliable sensor calibration", applied to the low-cost NO_2 sensor described in section "Autonomous NO_2 monitoring platform: reference data acquisition". We provide an overview of the dataset used for verification experiments, summarize the results across different calibration procedure configurations, and present observations and findings.

Reference and raw sensor datasets

The composition of the datasets has been already discussed in section "Data acquisition". For additional illustration, Fig. 15 showcases selected subsets of the reference and raw (uncorrected) low-cost sensor training data. It is important to note the considerable disparities between the reference and the sensor NO_2 readings,

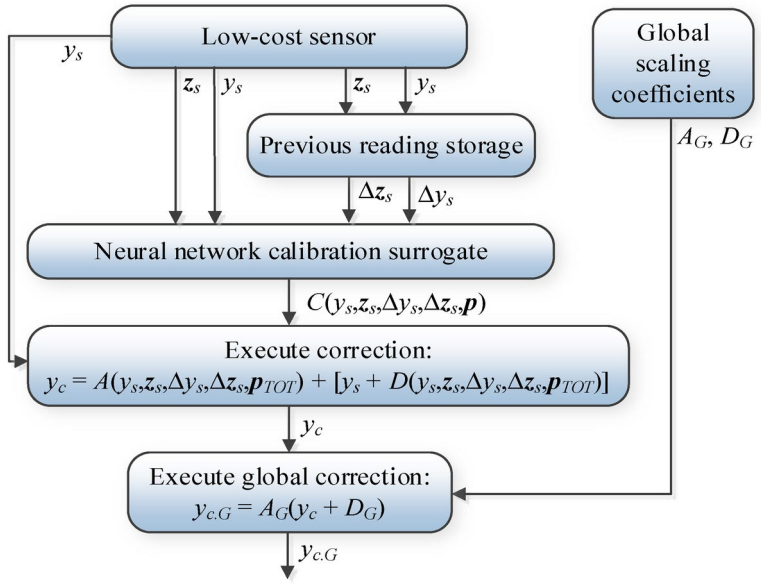

Fig. 14. Operating flow of the proposed low-cost sensor calibration procedure. (Local) calibration coefficients are generated using the NN surrogates based on the auxiliary vector z_s, the actual NO_2 reading y_s from the low-cost sensor, as well as their differentials The affine correction is then applied to the sensor reading to produce the outcome y_c. Subsequently, global data scaling is superimposed to produce the final corrected reading $y_{c.G}$.

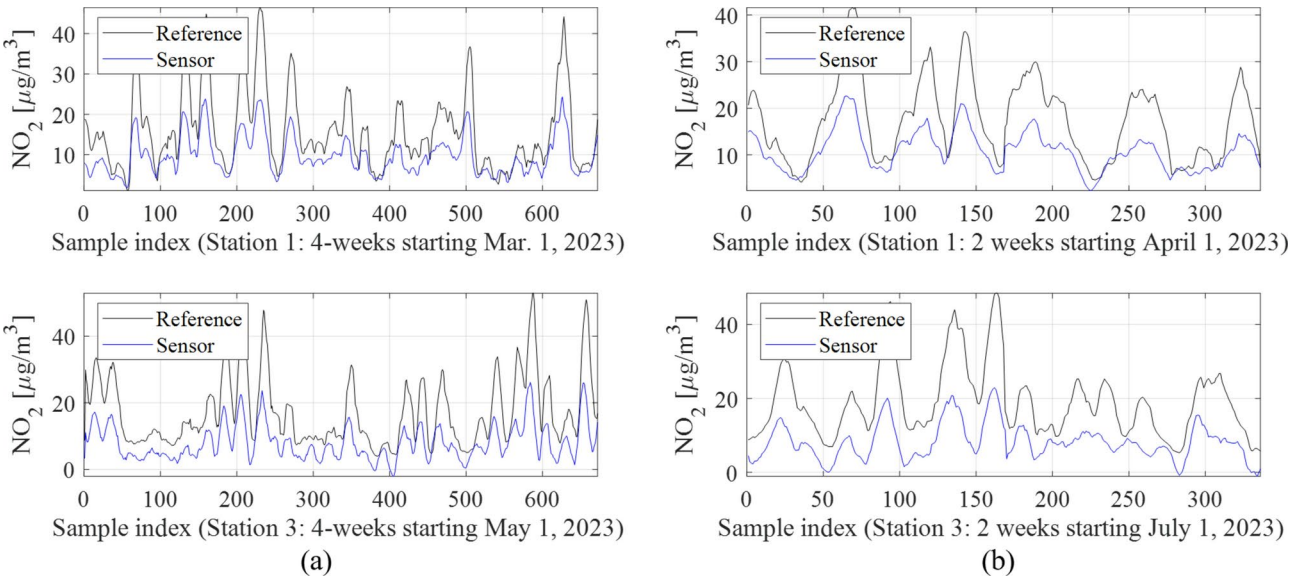

Fig. 15. Selected subsets of NO_2 readings from the reference stations and the respective low-cost sensors: (**a**) training data, (**b**) testing data.

making the calibration process a challenging task. In particular, the RMSE for the raw low-cost data (w.r.t. the reference) is as high as 8.9 $\mu g/m^3$, whereas the correlation coefficient is only 0.064.

Results

The low-cost NO_2 sensor, integrated into the autonomous monitoring platform outlined in section "Autonomous NO_2 monitoring platform: reference data acquisition", underwent calibration using the methodology detailed in section "Machine learning and global data scaling for reliable sensor calibration", utilizing data described in section "Reference and raw sensor datasets". To explore the significance of specific algorithmic elements within the correction scheme, various calibration scenarios were examined, as listed in Table 1. These configurations represent different combinations of surrogate model inputs (restricted or full auxiliary sensor parameters, utilization of NO_2 readings y_s from the primary sensor, utilization of differentials) and the inclusion of global

Calibration scenario	Calibration input variables				Global data correlation enhancement
	Auxiliary data	NO_2 reading from primary sensor (y_s)	Differentials Δz_s	Differentials Δy_s	
1	Restricted (only T_o, T_i, H_o, and H_i)	NO	NO	NO	NO
2	Restricted (z_s without pressure P)	NO	NO	NO	NO
3	Restricted (z_s without pressure P)	YES	NO	NO	NO
4	Complete z_s	YES	NO	NO	NO
5	Complete z_s	YES	NO	NO	YES
6	Complete z_s	YES	NO	YES	YES
7	Complete z_s	YES	YES	YES	NO
8	Complete z_s	YES	YES	YES	YES

Table 1. Calibration scenarios considered in validation studies.

Calibration scenario	Training data		Testing data			
					Absolute error	
	Correlation coefficient r	RMSE (µg/m^3)	Correlation coefficient r	RMSE (µg/m^3)	Mean (µg/m^3)	Interquarti e range (µg/m^3)
1	0.82	4.0	0.70	5.6	−1.7	7.5
2	0.89	3.0	0.81	4.3	−1.4	6.1
3	0.91	2.8	0.84	4.0	−1.0	5.6
4	0.93	2.5	0.86	3.9	−0.9	5.4
5	0.94	2.4	0.878	3.6	−0.5	4.8
6	0.93	2.6	0.886	3.4	−0.3	4.4
7	0.93	2.4	0.896	3.3	−0.3	4.1
8	0.94	2.3	0.903	3.17	−0.1	4.0

Table 2. Sensor calibration performance: correlation coefficients and RMSE.

data scaling. For each setup, the NN surrogate underwent ten training cycles, and the best-performing version (evaluated based on the mean-square error, MSE loss function on the training data) was chosen as the definitive model. Simultaneously, the affine scaling factor α (cf. section "Affine response correction of low-cost sensor") was adjusted, and a value of $\alpha = 0.8$ was determined as the most advantageous, ensuring the optimal approximation and generalization ability of the calibration models.

The findings from all scenarios are detailed in Table 2, showcasing the correlation coefficient and modeling error (RMSE) for both training and testing data (cf. Fig. 6 for relevant definitions). To maintain succinctness, only two scenarios are graphically represented. Figure 16 illustrates the reference and calibrated low-cost sensor NO_2 readings for the selected training and all testing data subsets for Scenario 2, along with scatter plots for both training and testing data. Similarly, Fig. 17 displays the same data for Scenario 8, representing our finalized calibration setup. Additionally, Fig. 18 provides a supplementary visualization for Scenarios 2 and 8, illustrating the combined training and testing outputs organized by ascending reference NO_2 readings, inclusive of reference NO_2 levels and corresponding raw and calibrated sensor readings.

Discussion and calibration procedure performance summary

The assessment in section "Results" is aimed at highlighting the effectiveness of the calibration process and gauging the performance of the rectified low-cost sensor, especially its reliability in nitrogen dioxide monitoring. Notably, sensor calibration is challenging due to significant differences between reference and sensor readings, along with a broad measurement dynamic range (ranging from nearly zero to approximately sixty µg/m^3), as depicted in Fig. 13. Furthermore, NO_2 levels often experience considerable fluctuations within short timeframes.

Despite the difficulties, the proposed calibration methodology demonstrates remarkable results, as evidenced by the correlation coefficients and RMSE provided in Table 2. Our optimal calibration setup, Scenario 8, incorporates a comprehensive range of input variables (all environmental parameters, NO_2 readings from both primary and supplementary sensors, and their respective differentials), along with global data scaling. This configuration achieves a correlation coefficient surpassing 0.9, with an impressively low RMSE of 3.17 µg/m^3 for the testing data. Considering the wide range of nitrogen dioxide levels recorded (from almost zero to about sixty µg/m^3), this error rate is noteworthy. The high accuracy of the corrected sensor is visually apparent in the alignment between its readings and the reference data, as depicted in Fig. 17.

It is important to highlight that each algorithmic component integrated into the calibration process significantly contributes to the overall accuracy of the corrected sensor. For instance, there is a marked improvement in the correlation coefficient and reduction in RMSE when the number of surrogate model inputs is increased (e.g., Scenario 7 versus 5 and 2). Likewise, incorporating the primary NO_2 sensor reading as a surrogate model input (Scenario 4 versus 2) enhances the correlation coefficient by approximately 0.05 and reduces RMSE by about 0.4 µg/m^3. Similarly, incorporating differentials (Scenario 7 versus 5) boosts the correlation coefficient by around

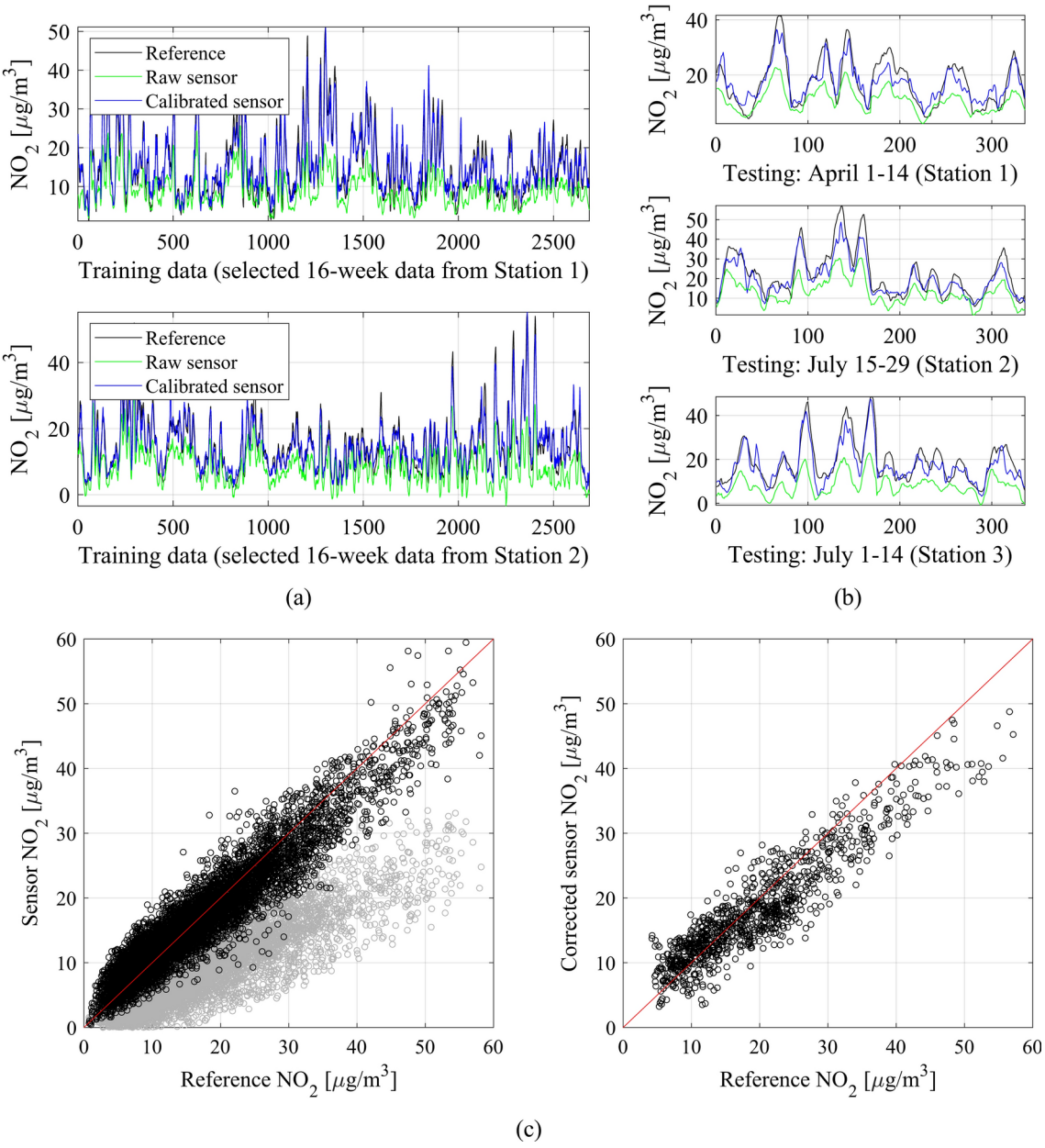

Fig. 16. Sensor calibration performance for Scenario 2 (cf. Table 1): (**a**) selected subsets of the training data; (**b**) collected testing data (reference—black, uncorrected sensor—green, corrected sensor—blue); scatter plots for the training data (left: uncorrected—gray, corrected—black) and the testing data (right).

0.02 and reduces RMSE by 0.3 to 0.4 μg/m^3. Lastly, global data scaling contributes to enhancing the correlation coefficient by nearly 0.02 and reducing RMSE by about 0.2 μg/m^3 (Scenario 5 versus 4, or 8 versus 7). These collective enhancements result in improved visual alignment between the reference and the calibrated low-cost sensor NO_2 readings. This improvement is evident in the scatter plots, notably more concentrated around the identity function for Scenario 8 (Fig. 17) compared to Scenario 2 (Fig. 16).

Furthermore, as it can be observed in Table 2, the mean value of the error for the testing data is relatively large for the simplest calibration setups, and it is gradually reduced to almost zero for the best configurations. The same can be said about the interquartile range, which quantifies the spread of the data. The employment of all proposed correction mechanisms reduced the range to about half of its initial value. On the other hand, the interquartile range is generally low, which means that the data dispersion is limited, and the majority of samples are associated with small values of the measurement error.

Figure 18 visually demonstrates the reliability enhancements achieved through the proposed calibration scheme by organizing the combined training and testing data based on increasing reference NO_2 readings. Notably, the corrected low-cost sensor readings are noticeably closer to their respective reference data compared to the raw sensor. A clear distinction is visible between Scenario 8 (Fig. 18b) and Scenario 2 (Fig. 18a), favouring

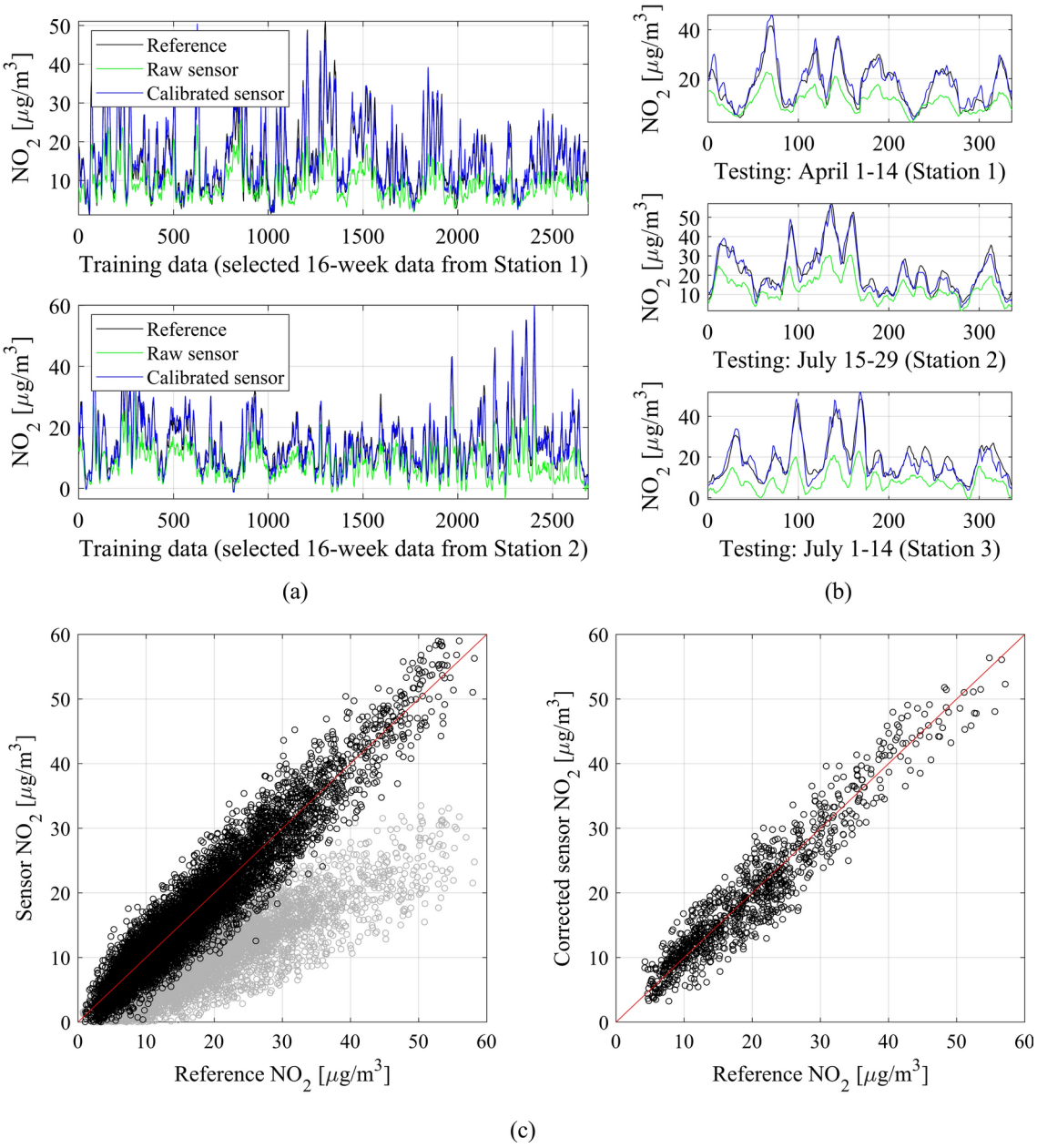

Fig. 17. Sensor calibration performance for Scenario 8 (cf. Table 1): (**a**) selected subsets of the training data; (**b**) collected testing data (reference—black, uncorrected sensor—green, corrected sensor—blue); scatter plots for the training data (left: uncorrected—gray, corrected—black) and the testing data (right).

the former. In Scenario 8, a substantial reduction in offset is evident, along with smaller disparities between the reference and the calibrated sensor readings, particularly noticeable at lower NO_2 levels. This results in smaller relative errors, averaging below fifteen percent for Scenario 8, in contrast to over twenty percent for Scenario 2.

Figure 19 displays the histograms representing the absolute errors (i.e., the discrepancies between the reference and the calibrated sensor NO_2 readings, y_r–y_c, across the entire testing dataset) for Scenarios 2 and 8. As anticipated, the error distribution approximates a normal curve. However, in Scenario 2, the mean error is negative (-1.4 μg/m^3), attributed to a certain asymmetry in the NO_2 reading distribution concerning the reference. This asymmetry is evident in the slightly skewed scatter plot (Fig. 16) and also visible in Fig. 18a regarding the offset. Contrastingly, in Scenario 8, due to the improved alignment with the reference and notably the global data scaling, the mean error converges near zero, resulting in a more symmetrical scatter plot accordingly.

The standard deviations for Scenarios 2 and 8 are 4.2 μg/m^3 and 3.1 μg/m^3, respectively. This substantial reduction demonstrates that refining the calibration method significantly enhances the reliability of the low-cost sensor. Analysing the data show that the calibrated sensor's absolute error to fall within 3 μg/m^3 with the

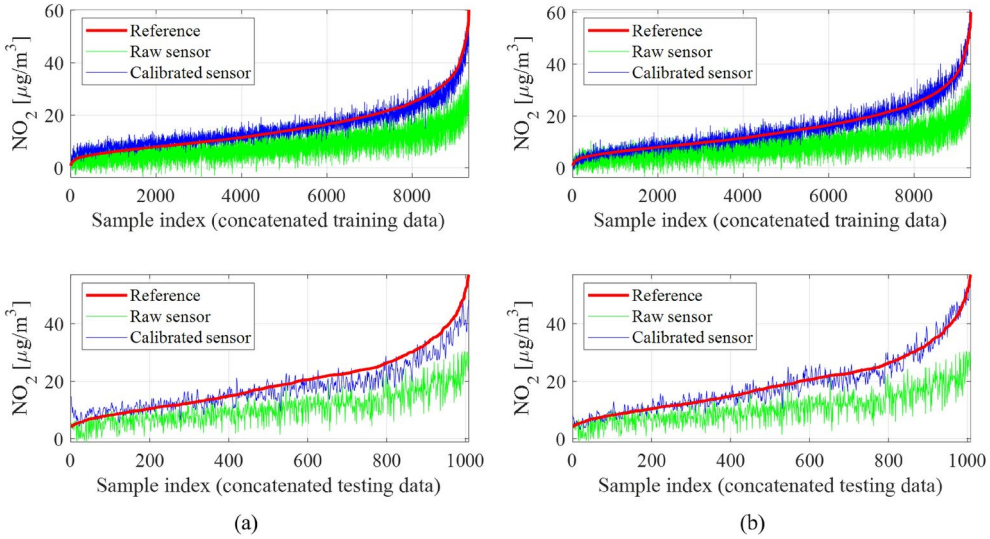

Fig. 18. Performance of sensor calibration for: (**a**) Scenario 2, (**b**) Scenario 8 (ultimate calibration scheme). The visualizations showcase the complete training dataset (top) and testing dataset (bottom), organized in ascending order based on NO_2 reference readings. These visuals underscore the significant improvement brought about by calibration, notably positioning the calibrated sensor readings much closer to their respective reference measurements compared to the raw data.

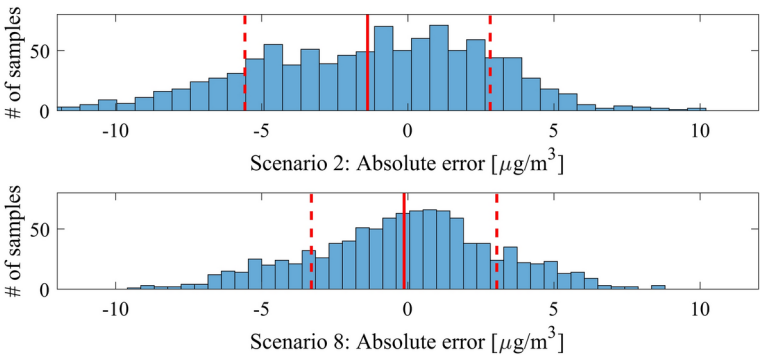

Fig. 19. Histograms of the absolute error $y_r - y_c$ (reference versus calibrated sensor) for concatenated testing samples (values in μg/m^3): (top) Scenario 2 (mean: − 1.4, standard deviation: 4.2), (bottom) Scenario 8 (mean: − 0.1, standard deviation: 3.1). Solid vertical lines mark the distribution means, whereas dashed lines denote standard deviations (w.r.t. the means).

likelihood of about 68%. Moreover, there is a higher probability of approximately 95% for the error to be within the range of ± 6 μg/m^3.

As corroborated by the discussed results, the calibrated low-cost sensor demonstrates exceptional reliability, especially when employing the most advanced correction scheme, Scenario 8, selected as the ultimate method. Practically, the calibration can be performed offline, applied to the NO_2 readings stored in the cloud after acquisition from the measurement platform. Alternatively, it can be integrated into the platform itself, utilizing the on-board computational facilities detailed in section "Autonomous NO_2 monitoring platform: reference data acquisition".

Conclusion

This article introduced a novel methodology for accurately calibrating low-cost nitrogen dioxide sensors. Our technique combines additive and multiplicative adjustments of the low-cost sensor readings with machine learning tools, particularly artificial neural networks (NNs). The NN surrogate is established to predict correction coefficients based on available auxiliary data, which includes environmental variables like temperature, humidity, atmospheric pressure, alongside NO_2 measurements from supplementary sensors, and their differentials. Surrogate-assisted calibration scheme is complemented by global data scaling procedure operating upon the complete training datasets. The proposed methodology has been applied to a custom-designed autonomous

monitoring platform equipped with primary and secondary NO_2 detectors, multiple environmental sensors, and dedicated electronic circuits for managing measurement protocols and wireless data transmission.

The calibration process utilized data from reference and low-cost sensors collected over five months in various locations across Gdansk, Poland. These monitoring platforms provided hourly output data for analysis, enabling extensive validation experiments. The calibration methodology showcased impressive reliability in NO_2 monitoring, boasting a correlation coefficient exceeding 0.9 w.r.t. the reference data, while maintaining a measurement error (RMSE) below 3.2 $\mu g/m^3$. This high level of accuracy solidifies the practicality and dependability of low-cost NO_2 detection. Comparative experiments, focusing on restricted calibration scenarios, underscored the significance of the incorporated correction mechanisms. Notably, augmenting the number of input variables, encompassing differentials, and implementing global data scaling synergistically enhanced the accuracy of low-cost sensor measurements.

In future endeavors, improving the reliability of NO_2 monitoring remains a primary goal. This includes integrating more gas detectors, such as SO_2, CO, and O_3, into the measurement platform. Their readings will serve as supplementary inputs for refining the calibration model, exploring cross-sensitivity, and enhancing overall accuracy. Moreover, the focus will shift toward advanced machine learning methods, especially deep learning models. Integrating these with regression strategies aims to further fine-tune and improve the calibration process.

Data availability

The datasets used and/or analysed during the current study available from the corresponding author on reasonable request.

Received: 30 December 2023; Accepted: 21 October 2024
Published online: 30 October 2024

References

1. Chen, T.-M., Kuschner, W. G., Gokhale, J. & Shofer, S. Outdoor air pollution: Nitrogen dioxide, sulfur dioxide, and carbon monoxide health effects. *Am. J. Med. Sci.* **333**(4), 249–256 (2007).
2. Zhao, S. et al. Assessing NO_2-related health effects by non-linear and linear methods on a national level. *Sci. Total Environ.* **744**, 140909 (2020).
3. Guerriero, C., Chatzikiakou, L., Cairns, J. & Mumovic, D. The economic benefits of reducing the levels of nitrogen dioxide (NO_2) near primary schools: The case of London. *J. Environ. Manag.* **181**, 615–622 (2016).
4. Kelly, F. J. & Fussell, J. C. Air pollution and airway disease. *Clin. Exp. Allergy* **41**(8), 1059–1071 (2011).
5. Schwela, D. Air pollution and health in urban areas. *Rev. Environ. Health* **15**(1–2), 13–42 (2000).
6. Salonen, H., Salthammer, T. & Morawska, L. Human exposure to NO_2 in school and office indoor environments. *Environ. Int.* **130**, 104887 (2019).
7. Agras, J. & Chapman, D. The Kyoto protocol, cafe standards, and gasoline taxes. *Contemp. Econ. Policy* **17**(3), 296–308 (1999).
8. Organization, W. H. *Air Quality Guidelines: Global Update 2005: Particulate Matter, Ozone Nitrogen Dioxide, and Sulfur Dioxide* (World Health Organization, Brazil, 2006).
9. OECD. *The Economic Consequences of Outdoor Air Pollution* (OECD Publishing, Paris, 2016).
10. Mauzerall, D. L., Sultan, B., Kim, N. & Bradford, D. F. NOx emissions from large point sources: Variability in ozone production, resulting health damages and economic costs. *Atmos. Environ.* **39**(16), 2851–2866 (2005).
11. Rodgers, M. O., Bradshaw, J. D. & Davis, D. D. Photofragmentation—Laser induced fluorescence detection of NO_2. In *Topical Meeting on Spectroscopy in Support of Atmospheric Measurements (1980), paper TuP17* (Optica Publishing Group, 1980).
12. Platt, U. Air monitoring by differential optical absorption spectroscopy. In *Encyclopedia of Analytical Chemistry: Applications, Theory, and Instrumentation* (ed. Meyers, R. A.) 1–28 (Wiley, 2007). https://doi.org/10.1002/9780470027318.a0706.pub2.
13. Matsumoto, J., Hirokawa, J., Akimoto, H. & Kajii, Y. Direct measurement of NO_2 in the marine atmosphere by laser-induced fluorescence technique. *Atmos. Environ.* **35**(16), 2803–2814 (2001).
14. Berden, G., Peeters, R. & Meijer, G. Cavity ring-down spectroscopy: Experimental schemes and applications. *Int. Rev. Phys. Chem.* **19**, 565–607 (2010).
15. Yu, H. et al. A deep calibration method for low-cost air monitoring sensors with multilevel sequence modeling. *IEEE Trans. Instrum. Meas.* **69**(9), 7167–7179 (2020).
16. Bi, J., Wildani, A., Chang, H. H. & Liu, Y. Incorporating low-cost sensor measurements into high-resolution $PM_{2.5}$ modeling at a large spatial scale. *Environ. Sci. Technol.* **54**, 2152–2162 (2020).
17. Castell, N. et al. Can commercial low-cost sensor platforms contribute to air quality monitoring and exposure estimates?. *Environ. Int.* **99**, 293–302 (2017).
18. Spinelle, L., Gerboles, M., Villani, M. G., Aleixandre, M. & Bonavitacola, F. Field calibration of a cluster of low-cost available sensors for air quality monitoring. Part A: Ozone and nitrogen dioxide. *Sens. Actuators B Chem.* **215**, 249–257 (2015).
19. Fonollosa, J., Fernández, L., Gutièrrez-Gálvez, A., Huerta, R. & Marco, S. Calibration transfer and drift counteraction in chemical sensor arrays using Direct Standardization. *Sens. Actuat. B-Chem.* **236**, 1044–1053 (2016).
20. Rai, A. C. et al. End-user perspective of low-cost sensors for outdoor air pollution monitoring. *Sci. Total Environ.* **607**, 691–705 (2017).
21. Kim, H., Müller, M., Henne, S. & Hüglin, C. Long-term behavior and stability of calibration models for NO and NO_2 low-cost sensors. *Atmos. Meas. Tech.* **15**, 2979–2992 (2022).
22. Poupry, S., Medjaher, K. & Béler, C. Data reliability and fault diagnostic for air quality monitoring station based on low cost sensors and active redundancy. *Measurement* **223**, 113800 (2023).
23. Carotta, M. C. et al. Nanostructured thick-film gas sensors for atmospheric pollutant monitoring: Quantitative analysis on field tests. *Sens. Actuators B Chem.* **76**(1–3), 336–342 (2001).
24. Wang, Z. et al. Improved deep bidirectional recurrent neural network for learning the cross-sensitivity rules of gas sensor array. *Sens. Actuators B Chem.* **401**, 134996 (2024).
25. Zimmerman, N. et al. A machine learning calibration model using random forests to improve sensor performance for lower-cost air quality monitoring. *Atmos. Meas. Tech.* **11**, 291–313 (2018).
26. Gorshkova, A. et al. Enhancement in NO_2 sensing properties of SWNTs: A detailed analysis on functionalization of SWNTs with Z-Gly-OH. *J. Mater. Sci.: Mater. Electron.* **34**, 102 (2023).
27. Jiao, W. et al. Community air sensor network (CAIRSENSE) project: Evaluation of low-cost sensor performance in a suburban environment in the southeastern United States. *Atmos. Meas. Tech.* **9**, 5281–5292 (2016).

28. Lewis, A. C. et al. Evaluating the performance of low cost chemical sensors for air pollution research. *Faraday Discuss.* **189**, 85–103 (2016).
29. Han, P. et al. Calibrations of low-cost air pollution monitoring sensors for CO, NO_2, O_3, and SO_2. *Sensors* **21**, 256 (2021).
30. Müller, M. et al. Integration and calibration of non-dispersive infrared (NDIR) CO_2 low-cost sensors and their operation in a sensor network covering Switzerland. *Atmos. Meas. Tech.* **13**, 3815–3834 (2020).
31. Shusterman, A. A. et al. The BeErkeley atmospheric CO_2 observation network: Initial evaluation. *Atmos. Chem. Phys. Discuss.* **16**, 13449–13463 (2016).
32. Andersen, T., Scheeren, B., Peters, W. & Chen, H. A UAV-based active AirCore system for measurements of greenhouse gases. *Atmos. Meas. Tech.* **11**, 2683–2699 (2018).
33. Kunz, M. et al. Surface flux estimates derived from UAS-based mole fraction measurements by means of a nocturnal boundary layer budget approach. *Atmos. Meas. Tech.* **13**, 1671–1692 (2020).
34. Bigi, A., Mueller, M., Grange, S. K., Ghermandi, G. & Hueglin, C. Performance of NO, NO_2 low cost sensors and three calibration approaches within a real world application. *Atmos. Meas. Tech.* **11**, 3717–3735 (2018).
35. Nowack, P., Konstantinovskiy, L., Gardiner, H. & Cant, J. Machine learning calibration of low-cost NO_2 and PM_{10} sensors: Non-linear algorithms and their impact on site transferability. *Atmos. Meas. Tech.* **14**, 5637–5655 (2021).
36. D'Elia, G. et al. Influence of concept drift on metrological performance of low-cost NO_2 sensors. *IEEE Trans. Instrum. Meas.* **71**, 1004811 (2022).
37. Jain, S., Presto, A. A. & Zimmerman, N. Spatial modeling of daily $PM_{2.5}$, NO_2, and CO concentrations measured by a low-cost sensor network: Comparison of linear, machine learning, and hybrid land use models. *Environ. Sci. Technol.* **55**(13), 8631–8641 (2021).
38. Ionascu, M.-E. et al. Calibration of CO, NO_2, and O_3 using Airify: A low-cost sensor cluster for air quality monitoring. *Sensors* **21**, 7977 (2021).
39. Bi, J. et al. Contribution of low-cost sensor measurements to the prediction of $PM_{2.5}$ levels: A case study in Imperial County, California, USA. *Environ. Res.* **180**, 108810 (2020).
40. van Zoest, V., Osei, F. B., Stein, A. & Hoek, G. Calibration of low-cost NO_2 sensors in an urban air quality network. *Atmos. Environ.* **210**, 66–75 (2019).
41. De Vito, S., Veneri, P.D., Esposito, E., Salvato, M., Bright, V., Jones, R.L., & Popoola, O., (2015). Dynamic multivariate regression for on-field calibration of high speed air quality chemical multi-sensor systems. In *XVIII AISEM Annual Conference*, Trento, Italy, 1–3.
42. Masson, N., Piedrahita, R. & Hannigan, M. Quantification method for electrolytic sensors in long-term monitoring of ambient air quality. *Sensors* **15**, 27283–27302 (2015).
43. Esposito, E. et al. Dynamic neural network architectures for on field stochastic calibration of indicative low cost air quality sensing systems. *Sens. Actuators B: Chem.* **231**, 701–713 (2016).
44. Wang, Z. et al. Self-adaptive temperature and humidity compensation based on improved deep BP neural network for NO_2 detection in complex environment. *Sens. Actuators B: Chem.* **362**, 131812 (2022).
45. BeagleBone® Blue, BeagleBoard, https://www.beagleboard.org/boards/beaglebone-blue.
46. SGX-7NO_2 Datasheet, Industrial Nitrogen Dioxide (NO_2) Sensor', SGX Sensortech. https://www.sgxsensortech.com/content/uploads/2021/10/DS-0338-SGX-7NO2-datasheet.pdf
47. Four Electrode NO_2 Sensor, SemaTech (7E4-NO_2-5) (PN: 057-0400-200), SemeaTech Inc. https://www.semeatech.com/uploads/datasheet/7series/057-0400-200_EN.pdf
48. Datasheet MiCS-2714 1107 rev 6, SGX Sensortech. https://www.sgxsensortech.com/content/uploads/2014/08/1107_Datasheet-MiCS-2714.pdf
49. Humidity Sensor BME280, Bosch Sensortec. https://www.bosch-sensortec.com/products/environmental-sensors/humidity-sensors-bme280/
50. ARMAG Foundation: Home. https://armaag.gda.pl/en/index.htm
51. Vang-Mata, R. (ed.) *Multilayer Perceptrons* (Nova Science Pub. Inc., New York, 2020).
52. Dlugosz, S. *Multi-layer perceptron networks for ordinal data analysis* (Logos Verlag, Berlin, 2008).
53. Hagan, M. T. & Menhaj, M. Training feed-forward networks with the Marquardt algorithm. *IEEE Trans. Neural Netw.* **5**(6), 989–993 (1994).
54. Hazenkamp-von Arx, M. E. et al. $PM_{2.5}$ and NO_2 assessment in 21 European study centres of ECRHS II: Annual means and seasonal differences. *Atmos. Environ.* **38**, 1943–1953 (2004).
55. Breysse, P. N. et al. Indoor exposures to air pollutants and allergens in the homes of asthmatic children in inner-city Baltimore. *Environ. Res.* **98**, 167–176 (2005).
56. The Math Works Inc., MATLAB, version 2021a, Natick, MA (2021).
57. Map data from OpenStreetMap. http://openstreetmap.org/copyright

Acknowledgements

The research leading to these results has received funding from the Norway Grants 2014-2021 via the National Centre for Research and Development, Grant NOR/POLNOR/HAPADS/0049/2019-00. This work was also supported in part by the Icelandic Centre for Research (RANNIS) Grant 217771. The authors would also like to thank the Agency of Regional Atmospheric Monitoring Gdansk-Gdynia-Sopot (ARMAG) for providing free of charge data from the reference measurement stations.

Author contributions

S.K.: development of concept, methodology, software and numerical results, validation, writing original manuscript, funding acquisition; A.P.D.: development of concept, methodology, manuscript corrections; M.W.: project supervision, hardware development, funding acquisition, manuscript corrections; B.P.: hardware development, software drivers, validation, funding acquisition, manuscript corrections;

Declarations

Competing interests

The authors declare no competing interests.

Additional information

Correspondence and requests for materials should be addressed to S.K.